nature materials

ARTICLES

PUBLISHED ONLINE: 28 SEPTEMBER 2015 | DOI: 10.1038/NMAT4429

Reversible dilatancy in entangled single-wire materials

David Rodney[1,2*], Benjamin Gadot[2,3], Oriol Riu Martinez[3], Sabine Rolland du Roscoat[3] and Laurent Orgéas[3]

Designing structures that dilate rapidly in both tension and compression would benefit devices such as smart filters, actuators or fasteners. This property however requires an unusual Poisson ratio, or Poisson function at finite strains, which has to vary with applied strain and exceed the familiar bounds: less than 0 in tension and above 1/2 in compression. Here, by combining mechanical tests and discrete element simulations, we show that a simple three-dimensional architected material, made of a self-entangled single long coiled wire, behaves in between discrete and continuum media, with a large and reversible dilatancy in both tension and compression. This unusual behaviour arises from an interplay between the elongation of the coiled wire and rearrangements due to steric effects, which, unlike in traditional discrete media, are hysteretically reversible when the architecture is made of an elastic fibre.

Entangled fibrous materials are ubiquitous in nature and technology and include for instance biopolymer networks[1], organic and inorganic wools[2,3], carbon nanotube networks[4] and fibrous scaffolds[5]. They represent a class of emerging materials referred to as architectured[6] or architected[7] because their mechanical properties after scaling strongly depend on the geometry of their internal structure.

The stress–strain response of fibrous materials has been widely studied, and is often characterized by a pronounced strain stiffening in compression with a large hysteresis on decompression[2,5,8,9]. A less-explored property is their volume variation under deformation. This property may be quantified by Poisson's ratio, or in the case of finite strains, Poisson's function[10], defined during a uniaxial test as the negative ratio of the incremental lateral to axial strains. In the case of transversely isotropic materials, we have $\nu = -(\mathrm{d}L/L)/(\mathrm{d}H/H)$ (see Fig. 1 for notation) and the corresponding volumetric strain is $\mathrm{d}V/V = (1-2\nu)\mathrm{d}H/H$.

Most common materials have Poisson's ratios between 0 and 1/2 (refs 11,12), although we know a number of auxetic materials with negative Poisson's ratios[13,14]. In uniaxial tension, auxetic materials counterintuitively expand laterally and thus dilate more rapidly than common materials. Fibrous examples include sintered fibre networks[4,15–17] and spiral wire structures[18]. Much more rare are materials with a Poisson ratio above 1/2 (refs 19–22). They are called stretch densifiers[19] because they shrink laterally in tension so rapidly that their volume decreases, but they could equally be called compressive dilatant because they expand laterally so rapidly in compression that their volume increases. So far, in the absence of internal transformation such as protein unfolding[12,23], only carbon nanotube yarns[24] and aerogel sheets[25] have been reported as stretch densifiers.

At finite strains, an increase in volume during compression is the well-known dilatancy[26–28], characteristic of plastic flow in granular and other discrete systems[29], where steric-induced plastic events create a free volume that decreases the network compacity. In these cases however, dilatancy is irreversible. Its strength has been characterized by a parameter that is, which is just twice the Poisson function defined above, and was found in sands between 1 and 2 (refs 30,31).

Here, using a combination of mechanical tests, image analysis and discrete element simulations, we explore the Poisson function of entangled materials made of a single long fibre entangled with itself[32,33]. These single-wire materials have a simple, yet highly adaptable architecture in-between discrete and continuous media, resulting in the unexpected property of being both compressive dilatant and tensile auxetic with a Poisson function varying continuously from below 0 in tension to above 1 in compression. Also, when an elastic wire is used, the deformations are recoverable on unloading. Analysing the main deformation modes in the entanglements, these properties are explained by the combined effects of: elongation of the coiled fibre allowed by its finite equilibrium curvature; and steric effects, which limit or enhance local rotations of the coiled segments.

Entangled single-wire materials were processed using a series of thermomechanical treatments adapted from ref. 32. In summary, an initial straight wire is first shaped into a helix and then entangled with itself in a loose disordered ball, which is compressed into a cylinder (see Methods, ref. 34 and Supplementary Section I for details). The compression temperature is chosen high enough to set the shape of the sample and relax internal stresses but low enough to avoid sintering. Examples are shown in Fig. 1a,b. The numerical cut in the X-ray tomographic image in Fig. 1b illustrates the disordered entanglement of the coiled wire. This structure has an open-cell architecture similar to a foam and is highly ductile with high damping capabilities[32–35].

To separate the role of the architecture from the wire properties, we processed wires made from either a viscoelastic polymer (polyamide, PA), a superelastic shape-memory alloy (nickel–titanium, NiTi) or an elastoplastic metal (copper, Cu) (see Fig. 1a for an illustration). Using image analysis during uniaxial tension and compression cycles, we determined the evolution of the applied axial strain and of the lateral and volumetric strains in a gauge region

[1]Institut Lumière Matière, Université Lyon 1-CNRS, F-69622 Villeurbanne, France. [2]Université Grenoble Alpes-CNRS, SIMAP, F-38000 Grenoble, France. [3]Université Grenoble Alpes-CNRS, 3SR Lab, F-38000 Grenoble, France. *e-mail: david.rodney@univ-lyon1.fr

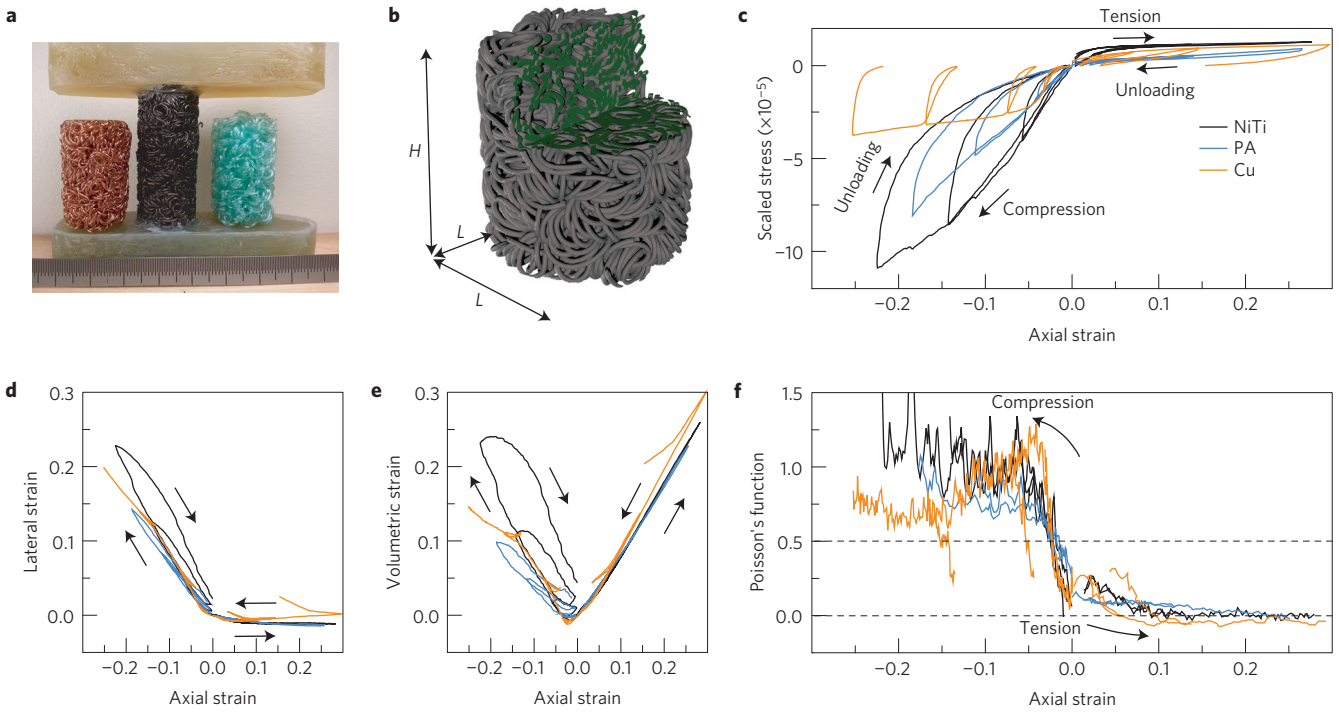

Figure 1 | Experimental mechanical curves. a, Examples of samples made of Cu (left), NiTi (centre) and polyamide (right) wires. The NiTi sample has its ends impregnated in a thermoset resin to serve as clamps during tensile tests. **b**, X-ray tomographic image of a NiTi sample with a numerical cut to illustrate the internal homogeneity of the structure. As transerve isotropy is preserved throughout the deformations, a single lateral dimension, L, is used. Initial dimensions of the sample are $L_0 = 20$ mm and $H_0 = 35$ mm. **c**, Axial stress scaled by the wire's Young modulus as a function of applied axial strain, $\epsilon_H = \ln(H/H_0)$, during uniaxial compression and tension cycles of samples with 35% relative density and processed from nickel–titanium (NiTi), polyamide (PA) and copper (Cu) wires. **d**, Lateral strain, $\epsilon_L = \ln(L/L_0)$, obtained from image analysis during the deformation cycles. **e**, Volumetric strain, $\epsilon_V = \ln(V/V_0) = 2\epsilon_L + \epsilon_H$. **f**, Poisson's function, $\nu = -(\mathrm{d}L/L)/(\mathrm{d}H/H) = -\mathrm{d}\epsilon_L/\mathrm{d}\epsilon_H$. For the sake of clarity, Poisson's functions are shown only during loading phases, both in compression and tension. Dashed lines at 0 and 0.5 show the boundaries of usual Poisson's ratios.

away from the sample extremities to avoid edge effects (see Methods and ref. 34 for details). For all three wires, the nominal axial stress scaled by the wire's Young modulus is shown in Fig. 1c, along with the lateral and volumetric strains in Fig. 1d,e. In compression, the visco- and superelastic (PA and NiTi) wire entanglements show similar mechanical responses, with hysteretic stress–strain cycles and negligible residual axial strain after unloading, even for applied strains beyond 20% (see Supplementary Movie 1). The reason is that in the absence of permanent bonds at contact points, the wire, which deforms mainly elastically when made of PA and NiTi, can largely rearrange on deformation, therefore avoiding high localized plastic strains. Moreover, owing to the internal cohesion along the single fibre, this architecture has a noticeable mechanical response in tension compared with cohesion-less discrete systems, although tensile stresses are about an order of magnitude lower than compressive stresses (Fig. 1c). With the elastoplastic copper wire, because of the high ductility of this metal beyond its yield stress, scaled stresses are lower and there are large residual strains on unloading.

Considering the compression cycles, we see in Fig. 1d that lateral strains are positive, meaning that the samples expand laterally, as expected for common materials. More interesting are the volumetric strains in Fig. 1e, which should be negative under compression, but are instead positive and increase substantially during each cycle, apart from short initial consolidating transients. This volume increase is the signature of compressive dilatancy, which extends up to the maximum compressive strains considered here. Moreover, we see in Fig. 1e that most of the dilatancy is recovered on decompression of the PA and NiTi wire entanglements, with a maximum volume increase after unloading of 5%. The ductility of the Cu wire does not limit dilatancy during compression but induces large irreversible lateral and volumetric strains on decompression, as seen in Fig. 1e.

The reversible dilatancy seen with the PA and NiTi wires is highly atypical and results from the unique mixed discrete–continuous architecture of the entanglements (see Supplementary Section II for a comparison with a glass model). On the one hand, single-wire systems are made of a discrete fibre, which undergoes steric-induced rearrangements lowering the density like in typical discrete systems. On the other hand, the continuity along the single wire ensures, with a visco- or a superelastic wire, the development of sufficient elastic back stress in the wire to pull the structure back towards its initial configuration on unloading, thus allowing for a remarkable recoverable deformation.

In tension, we would expect negative lateral strains as in other usual materials, but instead, we see in Fig. 1d that they are very close to zero with the PA and NiTi wires and even positive with the Cu wire. Thus, the entanglements do not shrink laterally in tension and expand in the case of the Cu wire. As a consequence, they dilate more rapidly than common materials and are even auxetic with the Cu wire. On decompression, the strains are again mostly recovered with the PA and NiTi wires, with negligible hysteresis compared with the compressions, whereas large residual strains are observed with the Cu wire due to its plasticity.

Entangled single-wire materials therefore dilate rapidly in both compression and tension, irrespective of the nature of the wire. The volume variations can be represented by Poisson's function shown in Fig. 1f. Poisson's function is strongly asymmetrical and strain-dependent: close to 0.1–0.2 near zero strain, Poisson's function increases in compression to exceed 1 (followed by a slight decrease

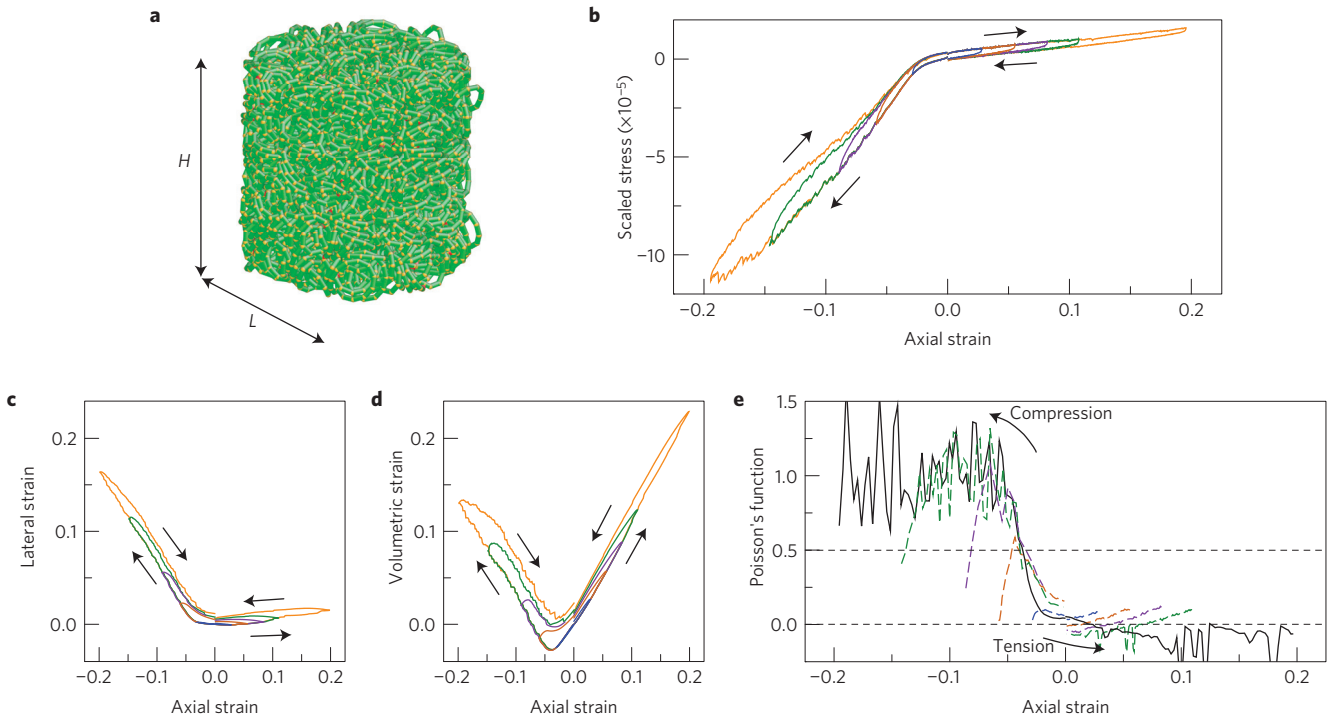

Figure 2 | Numerical mechanical curves on a cylindrical sample. a, Initial equilibrium configuration (visualized with Atomeye[48]), made of a single coiled fibre, discretized in 10,000 linear segments (green cylinders) separated by nodes (orange spheres). **b**–**e**, The same plots as in Fig. 1. In **e**, the loading curve is shown in black and some unloading curves appear as dashed coloured lines.

down to about 0.75 with the Cu wire), and decreases slowly in tension to become zero with the PA and NiTi wires, and slightly negative (∼−0.05) with the Cu wire. A Poisson function above 1/2 in compression is permitted elastically because the structure, which is isotropic at rest, becomes transversely isotropic under deformation (see Supplementary Section III for an *in situ* X-ray microtomographic study of the evolution under compression of the segment and contact orientation tensors).

To analyse more precisely the deformation mechanisms in the entanglements, and further isolate the role of the architecture, we performed discrete element simulations using a simple linear elastic constitutive law for the wire based on a discrete formulation of Kirchhoff's beam theory[36,37], with normal contact interactions[38] and no tangential friction. We produced numerical analogues of the experimental samples, reproducing the porosity, wire equilibrium curvature and sample dimensions (Fig. 2a). We controlled the altitude of the nodes near the top and bottom of the samples and simulated quasistatic uniaxial tension and compression cycles by applying strain increments in the vertical direction followed by energy minimizations (see Methods and Supplementary Section IV for details on the simulations and construction of the initial configuration).

The simulations shown in Fig. 2 reproduce the main features of the experiments of Fig. 1. Structurally, the evolution of the segment and contact orientations is similar to the experiments (see Supplementary Section III). The asymmetry between tension and compression is well predicted with comparable scaled stress levels (Fig. 2b). The hysteresis is smaller than experimentally, at least partly because of the absence of friction at self-contacts in the simulations. Reversible compressive dilatancy is also a straightforward outcome of the simulations, as seen in Fig. 2d. Slightly positive lateral strains are also predicted in tension (Fig. 2c). Finally, the resulting Poisson function in Fig. 2e shows a nonlinear behaviour close to the experiments: close to 0.05 at zero strain, Poisson's function increases rapidly in compression up to about 1 and decreases slowly in tension to become negative (∼−0.1 on average). The more negative Poisson function predicted in the simulations is probably due to the better entanglement obtained in the numerical samples, which is central to the variations of Poisson's function, as discussed below.

To ensure that the large tensile and compressive dilatancies are not artefacts of the finite size of the samples, we also performed simulations using periodic simulation cells that contain a single coiled wire, entangled with itself and coming in and out through the periodic boundary conditions (Fig. 3a). To simulate uniaxial tensions and compressions, one dimension of the cell was varied incrementally while the two other dimensions were adapted to maintain zero lateral tensile stresses (see Methods and Supplementary Section IV for details).

We recover again the tension–compression asymmetry (Fig. 3b) and large lateral and volumetric strain variations (Fig. 3c,d). It is also worth noting that successive cycles of deformation show discrete memory[39,40], with smaller cycles embedded in larger ones and the stresses and strains retracing previous cycles with fidelity (see Supplementary Section V). Discrete memory was also observed with the finite-size samples. This indicates the probable existence of Preisach-type bi-stable local configurations[41] in the entanglements, as in systems with internal transformations[12,23]. Also, with periodic boundary conditions, the variations of Poisson's function are larger and occur over a much narrower range of applied strains than with the finite-size samples (Fig. 3e): within ±2% of axial strain, Poisson's function increases above 1 in compression and decreases down to −0.25 in tension. Dilatancy in compression is therefore again confirmed and in tension, auxeticity is clearly marked. The reason is that periodic conditions allow for a more homogeneous wire entanglement without edge effects.

To further analyse Poisson's function variations, we performed two idealized simulations with periodic boundary conditions. First, we generated a sample with an equilibrium curvature 10 times smaller than the reference configuration. The corresponding

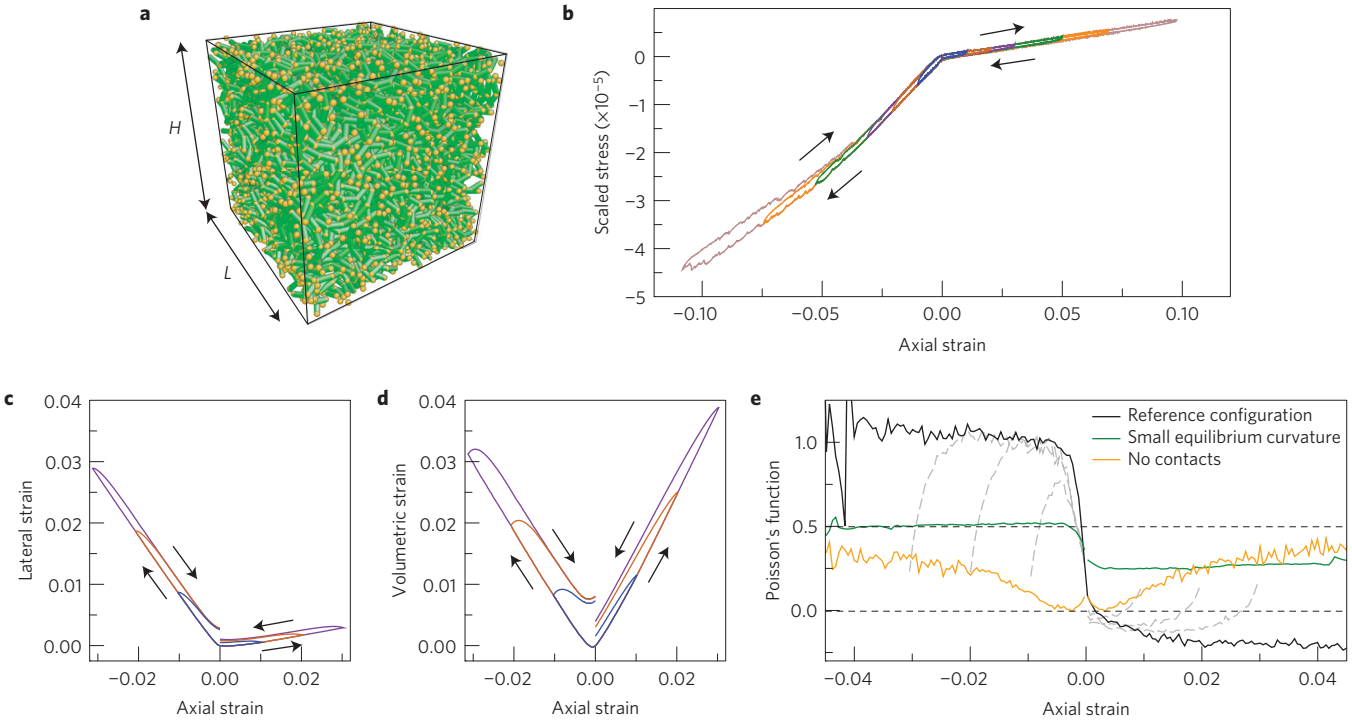

Figure 3 | Numerical mechanical curves on a periodic sample. a, Initial equilibrium configuration, made of a single coiled fibre, coming in and out of the simulation cell through the three-dimensional periodic boundary conditions. **b**–**e**, The same plots as in Figs 1 and 2. In **e**, also shown are the Poisson functions obtained during unloading (grey curves), on a configuration with a fibre equilibrium curvature 10 times smaller than the reference configuration (green curve) and when contacts between fibre segments are not accounted for (orange curve).

Poisson function, shown in green in Fig. 3e, varies only between 0.25 in tension and 0.5 in compression, that is, the network is now incompressible in compression and no longer auxetic in tension. In the second test, we started from the reference sample but did not account for fibre contacts, so that the fibre segments could cross each other freely. As shown in Fig. 3e (orange curves), tensions and compressions are then symmetrical and Poisson's function remains between 0 and 0.5.

Compressive dilatancy and tensile auxeticity require a finite equilibrium curvature and contacts between fibres. The reason is that both features are directly connected to the two main modes of deformation in the entanglements, namely the extension/compression of the wire coils and their rotation around contact points. To show this, we computed the axis vector of each elementary coil, defined as the end-to-end vector between nodes separated by one helical turn (see the inset in Fig. 4a). We measured during the simulations the change of average length ($\langle \ell \rangle$) and azimuthal angle ($\langle \phi \rangle$) of this vector. We see in Fig. 4a that the average coil extension as measured by the axis vector length varies much more rapidly in the reference architecture (black and orange curves) than when the equilibrium curvature is small (green curve). The reason is that coiled fibres can extend or contract like a spring, whereas straight fibres are inextensible.

In Fig. 4b, we show that the azimuthal angle increases in compression and decreases in tension because the coiled segments rotate perpendicularly (respectively, parallel) to the loading axis in compression (respectively, tension). In compression, the rotation is fastest in the reference architecture, reflecting that the creation of contacts in compression promotes fibre rotation, much like in a mikado game. This explains qualitatively the compressive dilatancy, which is known from the wine-rack model[19,42] to arise from fibre rotation, as illustrated on the right side of Fig. 4. In tension, fibre rotation is slowest when contacts are included, which also explains qualitatively the tensile auxeticity. Indeed, although auxeticity is mainly known to result from the unfolding of re-entrant structures, it may also arise in the case of limited rotation of stretchable fibres[4,42–44], as illustrated on the right side of Fig. 4.

The variations of $\langle \ell \rangle$ and $\langle \phi \rangle$ shown in Fig. 4 are difficult to predict with a simple mechanistic model because they depend on complex steric interactions difficult to represent without *ad hoc* parameters. In particular, it is difficult to account for the different nature of the contacts created in compression and tension. Contacts formed in compression are preferentially oriented vertically and contribute directly to the axial stress, whereas in tension, the contacts are mostly lateral (see Supplementary Section III). They resist a lateral collapse of the structure, but do not contribute directly to the axial stress, which explains the strong asymmetry between tension and compression when contacts are accounted for. However, even if we cannot simply predict the variations of $\langle \ell \rangle$ and $\langle \phi \rangle$, using only our measurement of their variations to constraint the kinematics of an 8-chain model[45] (see Fig. 4c and Supplementary Section VI) suffices to predict realistic Poisson's functions: as shown in Fig. 4d, we recover: the strong strain dependence of Poisson's function with the reference architecture; an almost constant Poisson function when the wire curvature is small; and a symmetrical Poisson function, starting at 0 and increasing with strain when contacts are not included. The model is not fully quantitative, as might be expected given its extreme simplicity, but it confirms that: compressive dilatancy arises from the combination of sterically induced fibre rotation and coil extension; and tensile auxeticity arises from the extension of stretchable coiled segments with limited rotation.

Finally, we studied the influence of the entanglement relative density and found on periodic samples with a fixed equilibrium curvature that below a critical relative density on the order of 33%, the entanglement is no longer sufficient to induce dilatancies (see Supplementary Section VII). We also expect compressive dilatancy to disappear at high relative densities because the very large number of initial contacts will not allow the fibre segments to rearrange

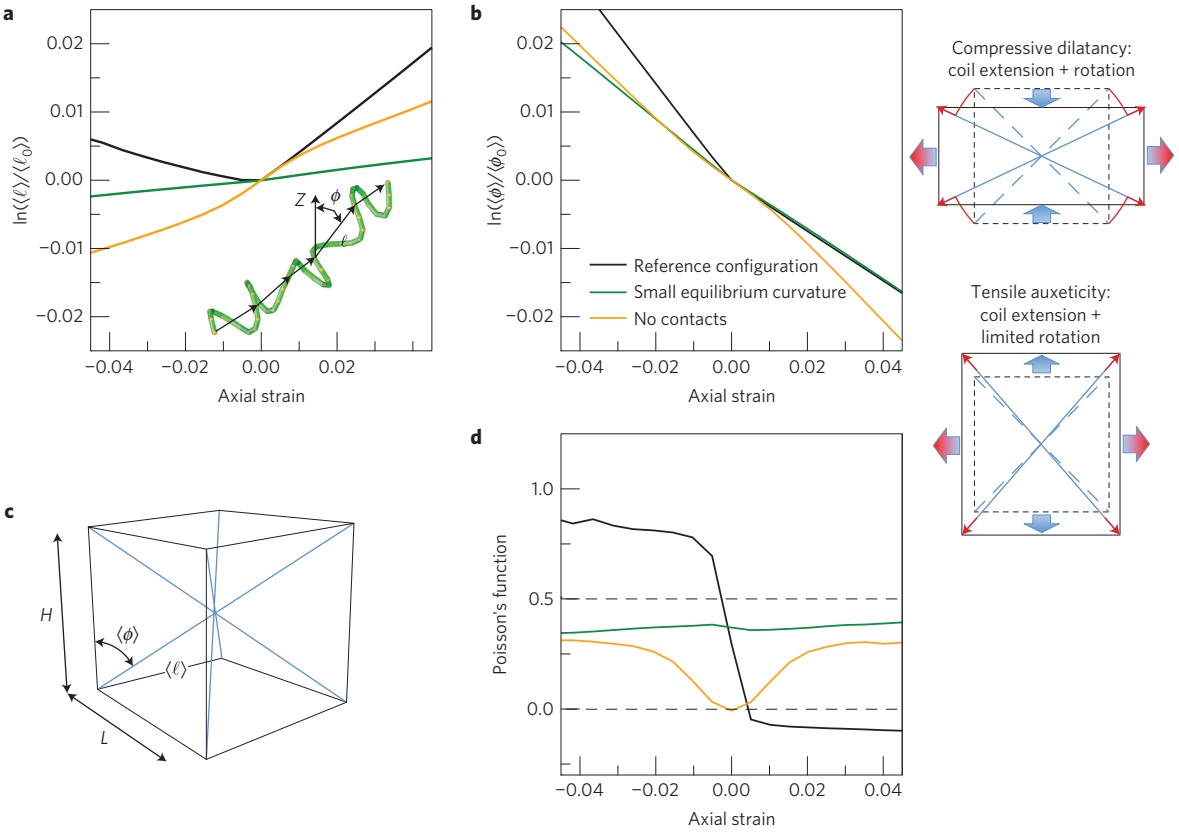

Figure 4 | Phenomenological 8-chain model. a,**b**, Coil deformations are measured by computing the change of average length (**a**) and average azimuthal angle (**b**) of the axis vector of each helical turn (end-to-end vector between nodes separated by 10 consecutive discrete segments, which corresponds to one turn in the initial helix). The same colour code is used as in Fig. 3e. **c**,**d**, This information is sufficient when used in an 8-chain model[45] (**c**) to predict Poisson's functions (**d**) in good agreement with the full calculations of Fig. 3. Within this model, $H=\langle\ell\rangle\cos\langle\phi\rangle$, $L=\langle\ell\rangle\sin\langle\phi\rangle/\sqrt{2}$ and Poisson's function is recomputed from $\nu=-(\mathrm{d}L/L)/(\mathrm{d}H/H)$ (see Supplementary Section VI for more details).

under deformation. As large curvatures also increase the number of initial contacts, unusual Poisson's functions are expected in a range of both intermediate densities and equilibrium curvatures. A more quantitative study is however left for a future publication. Also, we performed preliminary calculations including friction at contact points and observed that friction limits wire rearrangements and decreases compressive dilatancy (see Supplementary Section VIII).

To conclude, we have shown that entangled single-wire materials show a unique strain-dependent Poisson function, reflecting reversible dilatancy in both compression and tension. Poisson's functions above 1 in compression place this architecture among the most dilatant known discrete media[30,31]. This work opens the way to the design of adaptive architectures with varying porosity that could serve as strain-actuated filters, stress sensors, and fasteners, active under both tension and compression. Traditional auxetic materials for instance can be used in anchoring devices, but only in tension where they dilate, and not in compression where they shrink laterally rapidly. The same unidirectionality applies to stretch densifiers with the sign of the applied load reversed. Moreover, owing to the creation of new contacts on deformation, the present architecture does not suffer from softening, even if its relative density decreases. Several parameters can be optimized, such as the relative density and friction as mentioned above, but also at a given relative density, the fibre diameter and shape of the initial helix because, for instance, slanting is known to induce tensile auxeticity[46]. Finally, the architecture being fairly straightforward to construct, one may consider building it at different scales and in particular at the nanoscale to be used in nanodevices, for instance by entangling a carbon nanocoil[47].

Methods

Methods and any associated references are available in the online version of the paper.

Received 25 May 2015; accepted 25 August 2015;
published online 28 September 2015

References

1. Bao, G. & Suresh, S. Cell and molecular mechanics of biological materials. *Nature Mater.* **2,** 715–725 (2003).
2. Poquillon, D., Viguier, B. & Andrieu, E. Experimental data about mechanical behaviour during compression tests for various matted fibres. *J. Mater. Sci.* **40,** 5963–5970 (2005).
3. Masse, J. P., Salvo, L., Rodney, D., Bréchet, Y. & Bouaziz, O. Influence of relative density on the architecture and mechanical behaviour of a steel metallic wool. *Scr. Mater.* **54,** 1379–1383 (2006).
4. Hall, L. J. *et al.* Sign change of Poisson's ratio for carbon nanotube sheets. *Science* **320,** 504–507 (2008).
5. Laurent, C. *et al.* Mechanical behaviour of a fibrous scaffold for ligament tissue engineering: Finite elements analysis vs. X-ray tomography imaging. *J. Mech. Behav. Biol. Mater.* **40,** 222–233 (2014).
6. Ashby, M. Designing architectured materials. *Scr. Mater.* **68,** 4–7 (2013).
7. Zheng, X. *et al.* Ultralight, ultrastiff mechanical metamaterials. *Science* **344,** 1373–1377 (2014).
8. Barbier, C., Dendievel, R. & Rodney, D. Role of friction in the mechanics of nonbonded fibrous materials. *Phys. Rev. E* **80,** 016115 (2009).
9. Picu, R. C. Mechanics of random fiber networks—A review. *Soft Matter* **7,** 6768–6785 (2011).
10. Smith, C. W., Wootton, R. J. & Evans, K. E. Interpretation of experimental data for Poisson's ratio of highly nonlinear materials. *Exp. Mech.* **39,** 356–362 (1999).
11. Greaves, G. N., Greer, A. L., Lakes, R. S. & Rouxel, T. Poisson's ratio and modern materials. *Nature Mater.* **10,** 823–837 (2011).

12. Nicolaou, Z. G. & Motter, A. E. Mechanical metamaterials with negative compressibility transitions. *Nature Mater.* **11,** 608–613 (2012).
13. Lakes, R. Foam structures with a negative Poisson's ratio. *Science* **235,** 1038–1040 (1987).
14. Evans, K. E., Nkansah, M. A., Hutchinson, I. J. & Rogers, S. C. Molecular network design. *Nature* **353,** 124 (1991).
15. Delannay, F. Elastic model of an entangled network of interconnected fibres accounting for negative Poisson ratio behaviour and random triangulation. *Int. J. Solids Struct.* **42,** 2265–2285 (2005).
16. Tatlier, M. & Berhan, L. Modelling the negative Poisson's ratio of compressed fused fibre networks. *Phys. Status Solidi B* **246,** 2018–2024 (2009).
17. Neelakantan, S., Bosbach, W., Woodhouse, J. & Markaki, A. E. Characterization and deformation response of orthotropic fibre networks with auxetic out-of-plane behaviour. *Acta Mater.* **66,** 326–339 (2014).
18. He, G., Tan, Q., Jiang, G. & Li, Q. A novel mechanism for auxetic behavior in entangled materials with a spiral wire structure. *Smart Mater. Struct.* **23,** 095011 (2014).
19. Baughman, R. H., Stafström, S., Cui, C. & Dantas, S. O. Materials with negative compressibilities in one or more dimensions. *Science* **279,** 1522–1524 (1998).
20. Baughman, R. H. Auxetic materials: Avoiding the shrink. *Nature* **425,** 667 (2003).
21. Goodwin, A. L., Keen, D. A. & Tucker, M. G. Large negative linear compressibility of $Ag_3[Co(CN)_6]$. *Proc. Natl Acad. Sci. USA* **105,** 18708–18713 (2008).
22. Fortes, A. D., Suard, E. & Knight, K. S. Negative linear compressibility and massive anisotropic thermal expansion in methanol monohydrate. *Science* **331,** 742–746 (2011).
23. Brown, A. E., Litvinov, R. I., Discher, D. E., Purohit, P. K. & Weisel, J. W. Multiscale mechanics of fibrin polymer: Gel stretching with protein unfolding and loss of water. *Science* **325,** 741–744 (2009).
24. Zhang, M., Atkinson, K. R. & Baughman, R. H. Multifunctional carbon nanotube yarns by downsizing an ancient technology. *Science* **306,** 1358–1361 (2004).
25. Aliev, A. E. *et al.* Giant-stroke, superelastic carbon nanotube aerogel muscles. *Science* **323,** 1575–1578 (2009).
26. Reynolds, O. Dilatancy. *Nature* **33,** 429–430 (1886).
27. Onoda, G. Y. & Liniger, E. G. Random loose packings of uniform spheres and the dilatancy onset. *Phys. Rev. Lett.* **64,** 2727–2730 (1990).
28. Cates, M. E., Haw, M. D. & Holmes, C. B. Dilatancy, jamming, and the physics of granulation. *J. Phys. Condens. Matter* **17,** S2517–S2531 (2005).
29. Jaeger, H. M., Nagel, S. R. & Behringer, R. P. The physics of granular materials. *Phys. Today* **49,** 32–38 (April, 2008).
30. Rowe, P. W. The stress-dilatancy relation for static equilibrium of an assembly of particles in contact. *Proc. R. Soc. Lond. A* **269,** 500–527 (1962).
31. Bolton, M. D. The strength and dilatancy of sands. *Geotechnique* **36,** 65–78 (1986).
32. Tan, Q., Liu, P., Du, C., Wu, L. & He, G. Mechanical behaviors of quasi-ordered entangled aluminum alloy wire material. *Mater. Sci. Eng. A* **527,** 38–44 (2009).
33. Courtois, L. *et al.* Mechanical properties of monofilament entangled materials. *Adv. Eng. Mater.* **14,** 1128–1133 (2012).
34. Gadot, B. *et al.* Entangled single-wire NiTi material: A porous metal with tunable superelastic and shape memory properties. *Acta Mater.* **96,** 311–323 (2015).
35. Liu, P., He, G. & Wu, L. Uniaxial tensile stress–strain behavior of entangled steel wire material. *Mater. Sci. Eng. A* **509,** 69–75 (2009).
36. Antman, S. S. *Nonlinear Problems of Elasticity* Vol. 107, 63 (Applied Mathematical Sciences, Springer, 2005).
37. Bergou, M., Wardetzky, M., Robinson, S., Audoly, B. & Grinspun, E. Discrete elastic rods. *ACM Trans. Graph.* **27,** 63 (2008).
38. Rodney, D., Fivel, M. & Dendievel, R. Discrete modeling of the mechanics of entangled materials. *Phys. Rev. Lett.* **95,** 108004 (2005).
39. Ortin, J. Preisach modeling of hysteresis for a pseudoelastic CuZnAl single crystal. *J. Appl. Phys.* **71,** 1454–1461 (1992).
40. Guyer, R. A. & Johnson, P. A. Nonlinear mesoscopic elasticity: Evidence for a new class of materials. *Phys. Today* **52,** 30–36 (April, 1999).
41. Visintin, A. *Differential Models of Hysteresis* (Springer, 1994).
42. Grima, J. N., Attard, D., Caruana-Gauci, R. & Gatt, R. Negative linear compressibility of hexagonal honeycombs and related systems. *Scr. Mater.* **65,** 565–568 (2011).
43. Pikhitsa, P. V. Regular network of contacting cylinders with implications for materials with negative Poisson ratios. *Phys. Rev. Lett.* **93,** 015505 (2004).
44. Coluci, V. R. *et al.* Modeling the auxetic transition for carbon nanotube sheets. *Phys. Rev. B* **78,** 115408 (2008).
45. Arruda, E. M. & Boyce, M. C. A three-dimensional constitutive model for the large stretch behavior of rubber elastic materials. *J. Mech. Phys. Solids* **41,** 389–412 (1993).
46. Zhang, D. *et al.* Compression mechanics of nickel-based superalloy metal rubber. *Mater. Sci. Eng. A* **580,** 305–312 (2013).
47. Chen, X. *et al.* Mechanics of a carbon nanocoil. *Nano Lett.* **3,** 1299–1304 (2003).
48. Li, J. Atomeye: An efficient atomistic configuration viewer. *Modelling Simul. Mater. Sci. Eng.* **11,** 173–177 (2003).

Acknowledgements

This work was performed within the French National Research Agency (ANR) programmes 'Architectured NiTi materials' (ANIM, N.2010 BLAN 90201) with the support of LABEX Tec21 (ANR-11-LABX-0030) of Université Grenoble Alpes and LABEX iMUST (ANR-10-LABX-0064) of Université de Lyon (programme 'Investissements d'Avenir', ANR-11-IDEX-0007). D.R. acknowledges support from the Institut Universitaire de France and the Institute of Molecular Engineering of the University of Chicago. D.R. thanks J. de Pablo and H. Jaeger for fruitful discussions.

Author contributions

L.O. and D.R. conceived the study; B.G., O.R.M., S.R.d.R. and L.O. performed the experiments; D.R. developed the numerical code; B.G. and D.R. performed the simulations; all of the authors analysed the results; D.R. and L.O. wrote the manuscript.

Additional information

Supplementary information is available in the online version of the paper. Reprints and permissions information is available online at www.nature.com/reprints. Correspondence and requests for materials should be addressed to D.R.

Competing financial interests

The authors declare no competing financial interests.

Methods

Experiments. Single-wire materials were processed from wires made of commercial polyamide (PA) used for fishing lines (25wt% PA6 + 75wt% CoPA with 15% of PA66 sequences and 85% of PA6 sequences, commercialized by Caperlan), copper (Cu) used for electric wires and biomedical-grade nickel–titanium (Ni-50.8 at%Ti, commercialized by Fort Wayne Metals), with Young's moduli of 1.5, 126 and 60 GPa, respectively. All wires had the same diameter, 0.5 mm, and a length close to 20 m to yield an initial relative density of 35%. The processing route[32,34] (see ref. 34 and Supplementary Section I for more details) consists of: shaping the initial straight wire into a coil by rolling it around a threaded rod with a 3 mm diameter and a pitch close to the wire diameter, followed by a heat treatment at a temperature T_1; entangling the coil around a 3-mm-diameter rod to form a loose fibrous ball with disordered fibre placement and orientation; and compacting the ball in a cylindrical steel close die (diameter 20 mm), mounted on a mechanical testing machine (MTS DY34) equipped with a furnace to control the temperature at T_2. For the PA and NiTi wires, heat treatments were necessary to set the final shape and avoid internal stresses, whereas no heat treatment was needed with Cu because of its high ductility. For the PA wire, we used $T_1 = T_2 = 160\,^{\circ}\mathrm{C}$ for 15 min and 60 min, respectively. For the NiTi wire, both heat treatments lasted 2 min at $T_1 = T_2 = 350\,^{\circ}\mathrm{C}$. This temperature was adjusted to optimize the superelastic properties of the wire at room temperature. The sample dimensions are $L_0 = 20$ mm in diameter, and $H_0 \sim 35$ mm in height for the compression samples, and $\sim$45 mm for the tension samples. For those samples, an extra height of $\sim$5 mm was also added to impregnate the sample extremities in a thermoset polyester resin to serve as clamps (an illustration is shown in Fig. 1a,b). For each material, we produced a dozen samples, keeping the same helical geometry but changing the initial wire length to vary the final relative density. We present here only results at a relative density of 35%, which is the relative density mostly studied.

Uniaxial compression and tension cycles were performed at room temperature, with a strain rate of $4 \times 10^{-4}\ \mathrm{s}^{-1}$, inside a mechanical testing machine (MTS DY26). The applied force F was recorded to compute the nominal axial stress $4F/\pi L_0^2$. To avoid edge effects, strains were measured inside a gauge zone away from the sample extremities[34]. Images of the samples were acquired during deformation using a CCD (charge-coupled device) camera (Jai Pulnix RM-4200GE). Light reflections on wire segments on the external surface of the samples were used as reference points in combination with a particle tracking algorithm[49] to follow the deformation of a gauge zone, giving access to axial and lateral strains. The volumetric strain was deduced using the fact that the samples preserve their symmetry of revolution during deformation.

Discrete element calculations. Fibre mechanics was modelled using Kirchhoff's elastic beam theory[36] with a discretization scheme proposed in ref. 37. We used an in-house code available on request by contacting the corresponding author. Inextensibility was enforced by linear tensile springs inside each segment, and fibre contacts by repulsive potentials acting when the distance between any two segments becomes less that the fibre diameter[38]. The fibre diameter was 0.5 mm and the helix diameter 3.5 mm to match the experiments. Each helix turn was discretized in 10 segments with a total of 10,000 segments. The small curvature configuration was obtained with a larger helix diameter (350 mm) and fewer helical turns (10) discretized in 1,000 segments.

The cylindrical sample was constructed by first relaxing without contacts a tube of diameter 3.5 mm inside a cylinder of diameter 50 mm, modelled by a repulsive potential (Supplementary Section IV). A helix was then created inside the tube, which was again relaxed and compressed quasistatically including contacts to reach the final dimensions $L_0 = H_0 = 20$ mm. This structure was then set as an equilibrium initial configuration for the subsequent deformation cycles. With the periodic boundary conditions (Supplementary Section IV), we used a cubic cell (size L, with $L_0 = 20$ mm) and created the initial fibre as a toroidal helix of large diameter (2,000 mm) in a plane irrational with the cell faces. The periodic conditions then forced the initial torus to fold onto itself in the primary cell, creating numerous contacts between segments. This configuration was relaxed, keeping the cell dimensions fixed and the relaxed structure was set as an equilibrium initial configuration.

The configurations were incrementally deformed by increasing or decreasing the vertical cell dimension by small increments ($\pm 10^{-4}$ mm), followed by energy minimizations. With the cylindrical samples, we constrained the altitude of the nodes within two fibre diameters from the top and bottom surfaces. Forces on these nodes were used to compute the axial stress. Lateral and volumetric strains were obtained by sectioning the sample in thin slabs of height 5×10^{-3} mm and summing their surfaces and average radii extracted from Voronoi tessellations. With periodic boundary conditions, the vertical cell dimension was constrained, while the lateral dimensions were adapted to maintain zero lateral normal stresses. Stresses were obtained analytically from the Virial expression and strains from the evolution of the cell dimensions.

References

49. Schindelin, J. *et al.* Fiji: An open-source platform for biological-image analysis. *Nature Methods* **9,** 676–682 (2012).